

# Anomalous Shape Changes of Silicon Nanopillars by Electrochemical Lithiation

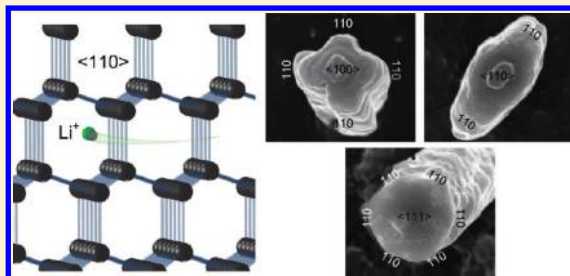
Seok Woo Lee,<sup>‡</sup> Matthew T. McDowell,<sup>‡</sup> Jang Wook Choi,<sup>†</sup> and Yi Cui<sup>\*</sup>

Department of Materials Science and Engineering, Stanford University, Stanford, California 94305, United States

**S** Supporting Information

**ABSTRACT:** Silicon is one of the most attractive anode materials for use in Li-ion batteries due to its  $\sim 10$  times higher specific capacity than existing graphite anodes. However, up to 400% volume expansion during reaction with Li causes particle pulverization and fracture, which results in rapid capacity fading. Although Si nanomaterials have shown improvements in electrochemical performance, there is limited understanding of how volume expansion takes place. Here, we study the shape and volume changes of crystalline Si nanopillars with different orientations upon first lithiation and discover anomalous behavior. Upon lithiation, the initially circular cross sections of nanopillars with  $\langle 100 \rangle$ ,  $\langle 110 \rangle$ , and  $\langle 111 \rangle$  axial orientations expand into cross, ellipse, and hexagonal shapes, respectively. We explain this by identifying a high-speed lithium ion diffusion channel along the  $\langle 110 \rangle$  direction, which causes preferential volume expansion along this direction. Surprisingly, the  $\langle 111 \rangle$  and  $\langle 100 \rangle$  nanopillars shrink in height after partial lithiation, while  $\langle 110 \rangle$  nanopillars increase in height. The length contraction is suggested to be due to a collapse of the  $\{111\}$  planes early in the lithiation process. These results give new insight into the Si volume change process and could help in designing better battery anodes.

**KEYWORDS:** Lithium-ion battery, silicon anode, phase change, anisotropic properties



Lithium-ion batteries have become a key component of portable electronic devices and electric vehicles as demand for smaller, lighter, and longer-lasting energy storage devices has increased.<sup>1,2</sup> Silicon is considered one of the most promising anode materials for Li-ion batteries because of its exceptional specific capacity of 4200 mAh g<sup>-1</sup>, which is about ten times that of commercial graphite anodes.<sup>3</sup> However, conventional Si anodes typically suffer from rapid capacity decay due to mechanical fracture caused by large volume expansion during the Li–Si reaction.<sup>4,5</sup> A recent notable achievement has been using Si nanostructures, such as nanowires, nanotubes, porous Si, and carbon-Si composites as battery anodes;<sup>6–11</sup> these nanostructures show improved resistance to fracture due to their small size and structural designs.<sup>12</sup>

At room temperature, the electrochemical alloying reaction of Li with crystalline Si involves a solid-state amorphization process concurrent with volume expansion.<sup>13,14</sup> Various ensemble methods, including X-ray diffraction and nuclear magnetic resonance, have been used to study the amorphization process;<sup>15–17</sup> these studies have primarily shown experimental evidence for the crystalline-to-amorphous phase transition and have also provided information on the local atomic structure of the amorphous phase. Computational studies have provided insights such as stable atomic arrangements and diffusion energy barriers.<sup>18,19</sup> In addition, atomic force microscopy has been used to show that volume expansion occurs during lithiation and contraction occurs during delithiation of Si thin films.<sup>5</sup> However, existing studies have not yet provided a clear understanding of the evolution of shape, volume, and atomic bonding during lithiation of Si nanostructures, which is critical for improving the performance of Si battery anodes. To understand this process, it

is necessary to investigate the physical nature of lithiation on a single-nanostructure level, which will reveal how the shape, volume, and bonding environment change during volume expansion. In this paper, we use Si nanopillars with three different axial orientations ( $\langle 100 \rangle$ ,  $\langle 110 \rangle$ , and  $\langle 111 \rangle$ ) as a model system to show that cross-sectional dimensional changes during lithiation are highly anisotropic and that both cross-sectional and axial dimensional changes depend on the crystalline orientation, all of which have never before been demonstrated. On the basis of our observations, we suggest a step-wise model for the structural changes that occur during the crystalline-to-amorphous transition in nanostructures.

For these experiments, we chose to use Si nanopillars fabricated by etching a Si wafer surface with SiO<sub>2</sub> nanospheres as an etch mask. These nanopillars present three advantages compared with other nanostructures for investigating morphological and structural changes in the crystal during reaction with Li. First, Si nanopillars with various axial crystalline orientations matching the orientations of the original Si wafers can be easily fabricated; nanopillars with axial orientations of  $\langle 100 \rangle$ ,  $\langle 110 \rangle$ , and  $\langle 111 \rangle$  are used in this study. Second, the nanopillars stand vertically on a fixed substrate, and the width and height of the pillars are uniform; this is important for comparing dimensional changes. Third, the crystalline directions of the nanopillar cross section can be easily defined during observations by tracking the orientation of the Si wafer substrate. Vertical Si nanopillars were fabricated on Si wafers by deep reactive-ion etching as shown in Supporting Information Figure S1.<sup>20,21</sup> After pillar fabrication, the

**Received:** May 26, 2011

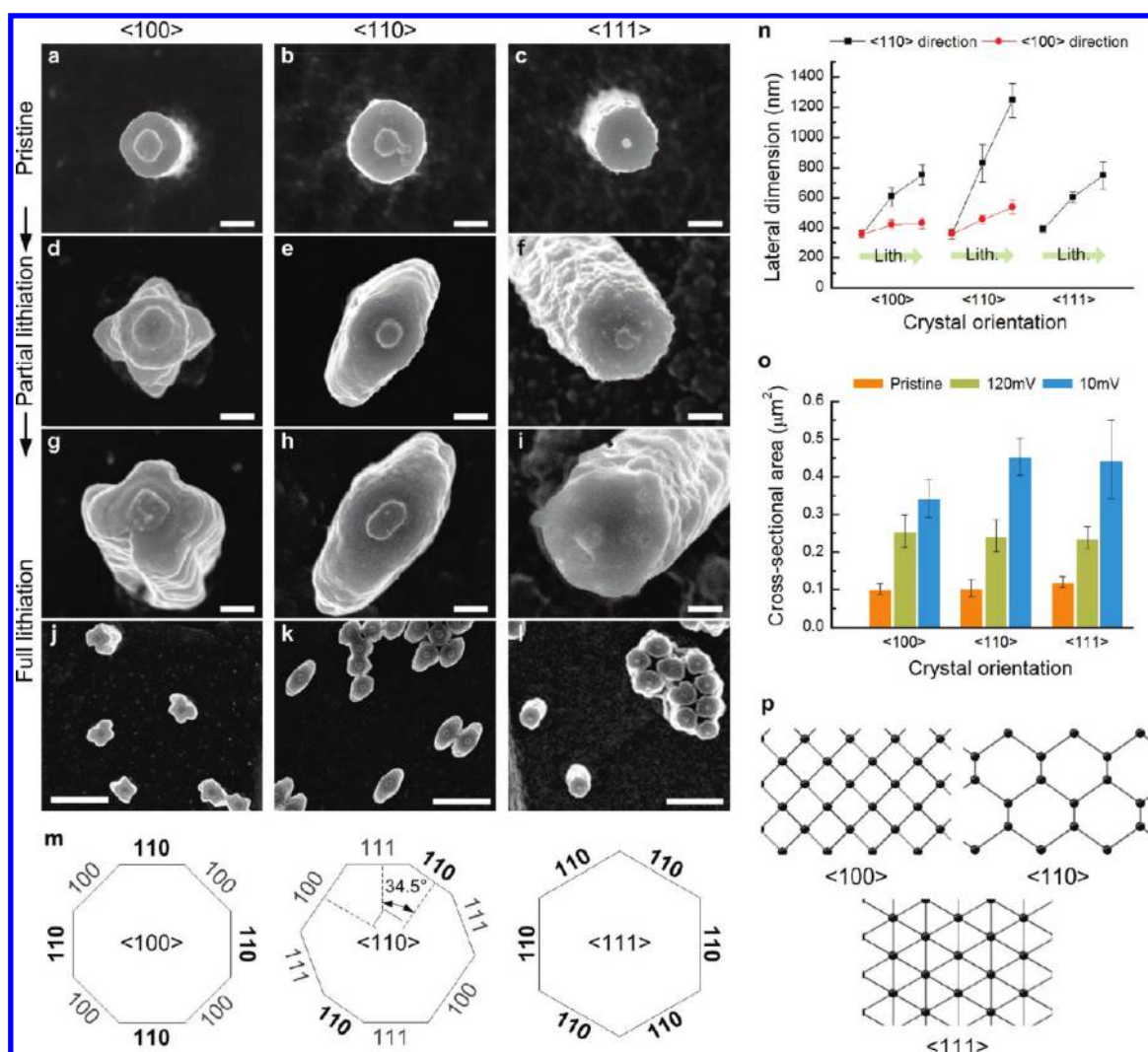


**Figure 1.** Anisotropic lateral expansion of crystalline Si nanopillars with three different axial orientations ( $\langle 100 \rangle$ ,  $\langle 110 \rangle$ , and  $\langle 111 \rangle$ ) upon lithiation. (a–i) Top-view SEM images of Si nanopillars of each crystal orientation and each lithiation state. The  $\langle 100 \rangle$  axially oriented pillars are shown in the left column,  $\langle 110 \rangle$  pillars are shown in the middle column, and  $\langle 111 \rangle$  pillars are shown in the right column. The top row shows pristine pillars, the second row shows partially lithiated pillars held at 120 mV vs Li/Li<sup>+</sup>, and the third row shows fully lithiated pillars held at 10 mV vs Li/Li<sup>+</sup>. The images in the fourth row show low-magnification views of fully lithiated pillars of each axial orientation. Scale bars from (a–i) are 200 nm and from (j–l) are 2  $\mu\text{m}$ . (m) Schematic diagram of the crystallographic orientation of the facets on the sidewalls of each of the pillars. Lithiated silicon primarily expands along the  $\langle 110 \rangle$  direction perpendicular to the nanopillar axis. (n) Statistical data of the changes in cross-sectional dimensions for the three types of nanopillars. Data is presented for pristine, partially lithiated, and fully lithiated pillars for cross-sectional expansion in both the  $\langle 110 \rangle$  and  $\langle 100 \rangle$  directions. (o) Statistical data of the changes in cross-sectional area for the three types of nanopillars. (p) View along three different directions of the diamond cubic lattice:  $\langle 100 \rangle$ ,  $\langle 110 \rangle$ , and  $\langle 111 \rangle$ . The  $\langle 110 \rangle$  direction presents the largest spacing between atoms.

piece of Si wafer on which the nanopillars stood was used directly as the working electrode in electrochemical half cells with Li metal foil as the counter electrode, as shown in Supporting Information Figure S2. We note that the underlying Si wafer can affect the specific capacity calculation, but it does not affect the observation of shape and volume changes in this study. The Si–Li electrochemical reaction was carried out by sweeping the voltage of the Si nanopillar electrode to a target voltage at a 0.1 mV/s sweep rate, and then it was held at the target voltage for at least 20 h to ensure equilibrium conditions exist within the nanopillars. The target voltages were 120 mV vs Li/Li<sup>+</sup> for partial lithiation and 10 mV vs Li/Li<sup>+</sup> for full lithiation.

Figure 1 contains top-view SEM images revealing how Si nanopillars with the three different axial orientations expand

laterally during lithiation. In the figure, the left column of images shows  $\langle 100 \rangle$  nanopillars, the middle column shows  $\langle 110 \rangle$  nanopillars, and the right column shows  $\langle 111 \rangle$  nanopillars. Individual nanopillars are shown in their pristine state (top row), partially lithiated by holding at 120 mV (second row), and fully lithiated by holding at 10 mV (third row). The first row of SEM images (Figure 1a–c) shows that the pristine Si nanopillars with different axial orientation all have a circular cross-section, which reflects the shape of the spherical nanospheres used as the etch mask. The use of 600 nm silica nanospheres results in a pillar diameter of about 400 nm due to side etching, and the slight difference of diameter in nanopillars with different orientations is caused by the different etching rate of the planes that make up the sidewalls. The button at the top of the nanopillars is the point at

which the silica sphere previously contacted the pillar. The second row of SEM images (Figure 1d–f) shows nanopillars partially lithiated by holding at 120 mV vs Li/Li<sup>+</sup>. These images show obvious anisotropic cross-sectional expansion. Specifically, the initially circular  $\langle 100 \rangle$ ,  $\langle 110 \rangle$ , and  $\langle 111 \rangle$  pillars transform to a cross, an ellipse, and a hexagon, respectively. With further lithiation to 10 mV versus Li/Li<sup>+</sup>, the nanopillars continue to expand anisotropically, and the cross and elliptical cross-sectional shapes of the  $\langle 100 \rangle$  and  $\langle 110 \rangle$  nanopillars become more significant, as shown in Figure 1g–i. At full lithiation, the cross section of the  $\langle 111 \rangle$  nanopillar (Figure 1i) is slightly hexagonal but is smeared out by the significant volume expansion. Finally, Figure 1j–l shows lower-magnification views of randomly distributed fully lithiated nanopillars, and it is clear that there is consistent anisotropic expansion of the individual nanopillars. Nanopillars in close contact are constrained by each other during volume expansion, resulting in complicated shape changes that are beyond the scope of this study.

From the SEM images in Figure 1, it seems that the nanopillars expand to a greater degree along a specific cross-sectional crystallographic direction of the pristine Si lattice. Figure 1m shows the crystallographic orientations of the sidewalls of the three different Si nanopillars, and it is clear that in all three cases the nanopillars expand most significantly along the  $\langle 110 \rangle$  family of directions. Along the  $\langle 110 \rangle$  direction, the crystalline Si structure presents relatively large interstitial spaces between atoms; this channel is much larger than those along the  $\langle 100 \rangle$  and  $\langle 111 \rangle$  directions. This is exhibited in Figure 1p, which shows schematics of the diamond cubic structure viewed along the  $\langle 100 \rangle$ ,  $\langle 110 \rangle$ , and  $\langle 111 \rangle$  directions. Because of the large space between atoms, the  $\langle 110 \rangle$  direction is a well-known ion channel in ion implantation processes.<sup>22</sup> We believe that this is also the case for lithium ions during electrochemical lithiation. In the  $\langle 100 \rangle$  axially oriented nanopillar, there are four  $\langle 110 \rangle$  directions perpendicular to the axis at 90° to each other (Figure 1m). In the  $\langle 110 \rangle$  nanopillar, there are two  $\langle 110 \rangle$  directions perpendicular to the axis opposite each other (Figure 1m). In the  $\langle 111 \rangle$  nanopillar, there are six  $\langle 110 \rangle$  directions perpendicular to the axis arranged hexagonally (Figure 1m). In contrast to the expansion along the  $\langle 110 \rangle$  directions, the nanopillars show very little cross-sectional expansion along  $\langle 100 \rangle$  or  $\langle 111 \rangle$  directions, which results in the observed anisotropic shape change in the  $\langle 100 \rangle$  and  $\langle 110 \rangle$  axially oriented pillars. Figure 1 panels n and o show statistical data of the cross-sectional dimension changes and area changes for each of the three nanopillar types. At least 30 nanopillars were measured for each average value, and the error bars represent the standard deviation. The  $\langle 100 \rangle$  and  $\langle 110 \rangle$  axially oriented pillars show similar expansion behavior during lithiation. The fully lithiated  $\langle 100 \rangle$  and  $\langle 110 \rangle$  axially oriented pillars expand by 111 and 245% along the  $\langle 110 \rangle$  cross-sectional direction but only 20 and 49% along the  $\langle 100 \rangle$  cross-sectional direction, respectively; this proves that lateral expansion along the  $\langle 100 \rangle$  direction is less significant than the  $\langle 110 \rangle$  direction. The  $\langle 111 \rangle$  pillars show quasi-isotropic lateral expansion during lithiation, so only the diameter was measured; this lateral dimensional change was 92%. Finally, the cross-sectional area of all three types of pillars increased considerably after lithiation: the  $\langle 100 \rangle$  pillars increased 240%, the  $\langle 110 \rangle$  pillars increased 340%, and the  $\langle 111 \rangle$  pillars increased 272%.

The cross-sectional expansion of amorphous lithiated silicon along the  $\langle 110 \rangle$  direction could be explained by considering fast diffusion along the  $\langle 110 \rangle$  direction and plastic deformation of the

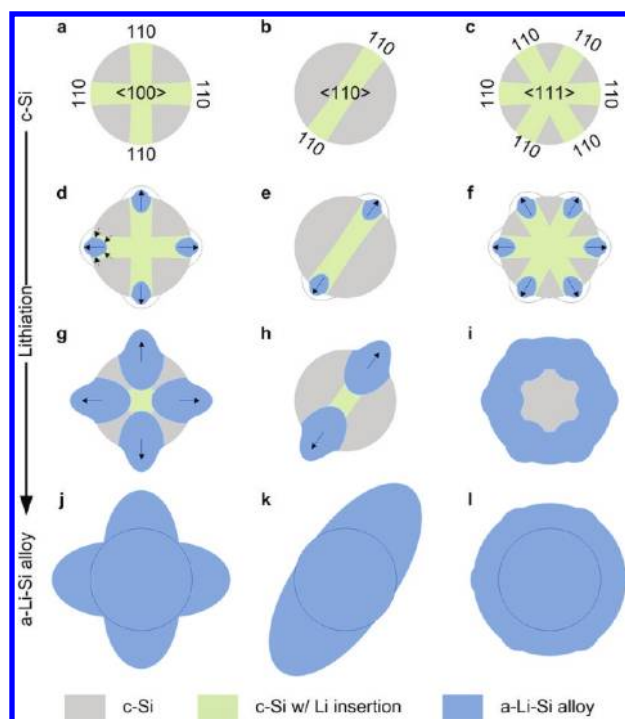


**Figure 2.** Schematic explaining anisotropic expansion of Si nanopillars. (a–c) Li diffuses along the  $\langle 110 \rangle$  lateral directions in each crystalline pillar. Green indicates the zones into which Li first diffuses. (d–f) Amorphization (blue) begins at the surface of the pillar along the  $\langle 110 \rangle$  directions due to the relatively high concentration of Li. The amorphized material is constrained by the surrounding crystalline regions and deforms. (g,h) With further lithiation, the  $\langle 100 \rangle$  and  $\langle 110 \rangle$  pillars still have crystalline regions remaining in the core and near the edges, and this directs the amorphous regions to continue expanding along the  $\langle 110 \rangle$  directions. (i) In the  $\langle 111 \rangle$  oriented pillar, the outer amorphous regions merge earlier in the lithiation process. (j,k) At full lithiation, the  $\langle 100 \rangle$  and  $\langle 110 \rangle$  axially oriented pillars expand to a cross shape and an ellipse as the amorphous regions are further displaced outward. (l) The  $\langle 111 \rangle$  pillar expands relatively isotropically.

amorphous Li–Si alloy, as shown in Figure 2. Since the  $\langle 110 \rangle$  crystallographic direction has larger channels than either the  $\langle 100 \rangle$  or  $\langle 111 \rangle$  directions, the energy barrier for Li diffusion is expected to be the lowest along the  $\langle 110 \rangle$  direction. So, as lithiation begins, the Li ions will begin to diffuse into the Si crystal from the nanopillar sidewalls along the  $\langle 110 \rangle$  directions (green zones in Figure 2), while there will be significantly less diffusion along the other lateral directions (light gray zones in Figure 2). This is shown schematically for the three different nanopillar orientations in Figure 2a–c. With further lithiation, amorphization of the Si crystal begins at the lateral ( $110$ ) surfaces where the concentration of lithium is the highest, as shown in Figure 2d–f (blue zones). Once the amorphous Li–Si alloy begins to expand in volume, it is pushed away from the crystalline–amorphous two-phase interface since the yield strength of the crystalline Si is much higher than that of the amorphous Li–Si alloy (our unpublished data has shown that the Li–Si alloy is significantly weaker than pure Si). As the amorphous region grows during further lithiation, the already-deformed Li–Si alloy is pushed further out, and the  $\langle 100 \rangle$ ,  $\langle 110 \rangle$ , and  $\langle 111 \rangle$  pillars begin to exhibit their unique cross-sectional lithiated shapes, as shown in the SEM images in Figure 1d–f. In the final stage of lithiation, the amorphous regions continue to grow along the  $\langle 110 \rangle$  directions,

but in the  $\langle 100 \rangle$  and  $\langle 110 \rangle$  axially oriented nanopillars, there are still crystalline regions that stretch from the core of the nanopillar to the edges along directions other than  $\langle 110 \rangle$ , as shown in Figure 2g,h. These directions maintain their mechanically rigid structure and do not expand. The end result for the  $\langle 100 \rangle$  and  $\langle 110 \rangle$  oriented pillars is that the Li–Si phase is extended along the  $\langle 110 \rangle$  lateral directions, while there is little expansion in the other directions since they are the last to be lithiated (Figure 2j,k). For the  $\langle 111 \rangle$  oriented nanopillar, however, there are six amorphous regions that are closer and can merge earlier in the lithiation process (Figure 2i). Once they are merged, the amorphous region becomes a shell surrounding the entire nanopillar, and the driving force for anisotropic deformation along the  $\langle 110 \rangle$  direction is lost, as evidenced by the SEM image in Figure 1i. The final cross-sectional shapes according to this analysis are shown in Figure 2j–l.

In order to fully understand the morphological changes during the Li–Si reaction, we also studied the height evolution of the nanopillars during lithiation. Figure 3 shows side-view SEM images of the three types of nanopillars in the pristine state, partially lithiated state (120 mV), and fully lithiated state (10 mV). Figure 3j presents statistics on the average height change for each type of nanopillar. First, it is observed that the percent change in height is at least an order of magnitude less than the percent change in cross-sectional dimension. This is because the cross section can undergo relatively unconstrained volume expansion due to the close proximity of free surfaces, while a significant height change is prevented by the constraint of the material along the axis. This anisotropy in axial versus cross-sectional dimensional change has previously been observed in Si nanotubes.<sup>10</sup> However, further analysis of the data in Figure 3j yields the completely unexpected result that the height of the  $\langle 110 \rangle$  pillars increases upon lithiation, while the height of the  $\langle 111 \rangle$  and  $\langle 100 \rangle$  pillars first decreases after partial lithiation to 120 mV and then increases during subsequent lithiation to 10 mV. The average height of the  $\langle 110 \rangle$  pillars increases by 0.7% after partial lithiation and 4.0% after full lithiation. However, the average height of the  $\langle 100 \rangle$  pillars shrinks by 4.3% after partial lithiation and then increases back to within 1% of the initial height after full lithiation, and the average height of the  $\langle 111 \rangle$  pillars shrinks by 9.5% after partial lithiation and then increases to 2.0% less than the initial height after full lithiation. For the  $\langle 111 \rangle$  pillars, this corresponds to an average height decrease of about 290 nm after partial lithiation, which is more than significant when compared to the error in the scanning electron micrograph scale bar ( $<20$  nm). The notable shrinking of the  $\langle 111 \rangle$  and  $\langle 100 \rangle$  nanopillars after partial lithiation is an unanticipated result, since expansion in all directions might be expected. Finally, Figure 3k shows the average volume changes for the three types of nanopillars. After full lithiation, the  $\langle 100 \rangle$ ,  $\langle 110 \rangle$ , and  $\langle 111 \rangle$  nanopillars undergo average volume expansion of 242.7, 270.8, and 264.3%, respectively. These values are similar and are all within about a standard deviation, as indicated by the error bars.

The height decrease in the  $\langle 111 \rangle$  and  $\langle 100 \rangle$  nanopillars could be explained by the partial collapse of  $\{111\}$  planes due to the breaking of Si–Si bonding between the planes by the insertion of lithium ions along  $\langle 110 \rangle$  ion channels. Related deformation has been investigated with regard to hydrogen implantation in Si.<sup>23–25</sup> Ab initio studies have shown that bonding between  $\{111\}$  planes can be broken by H atoms, and that this so-called “half stacking fault” has the lowest energy among possible crystal structures affected by hydrogen implantation.<sup>25</sup> In addition, experimental studies have shown microcrack propagation in Si

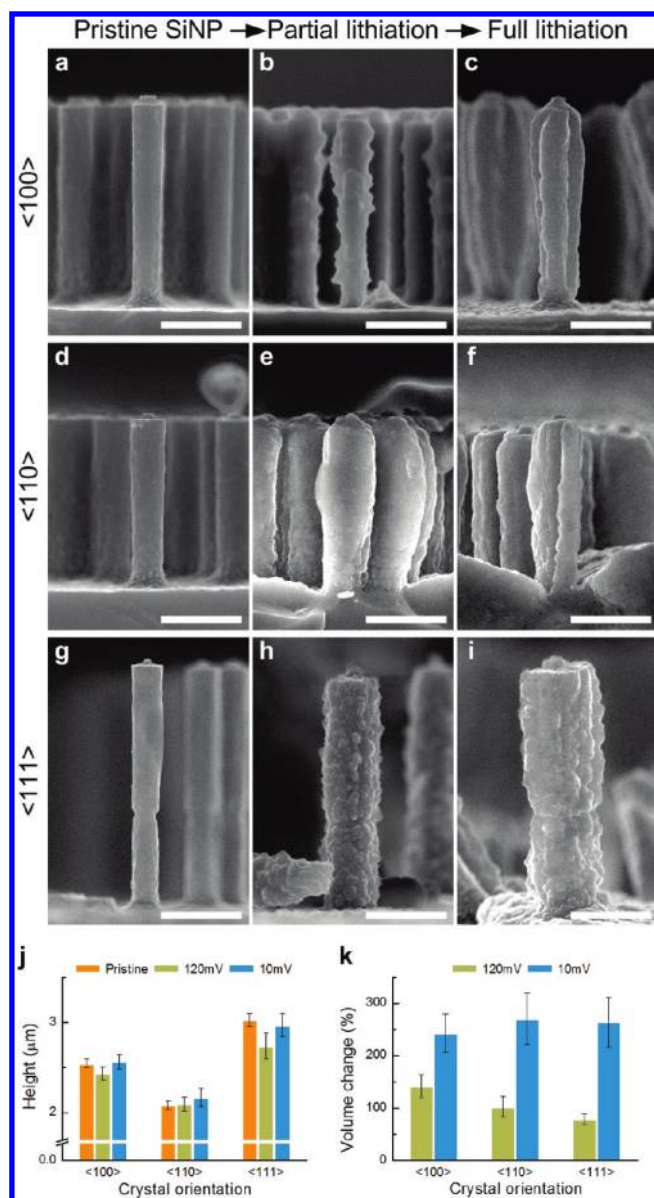


**Figure 3.** Length changes of crystalline Si nanopillars with three different axial orientations ( $\langle 100 \rangle$ ,  $\langle 110 \rangle$ , and  $\langle 111 \rangle$ ) upon lithiation. (a–i) Side-view SEM images of Si nanopillars of each crystalline orientation and each lithiation state at the same magnification. The  $\langle 100 \rangle$  pillars are shown in the top row,  $\langle 110 \rangle$  pillars are shown in the second row, and  $\langle 111 \rangle$  pillars are shown in the third row. The first column shows pristine pillars, the second column shows partially lithiated pillars held at 120 mV vs Li/Li<sup>+</sup>, and the third column shows fully lithiated pillars held at 10 mV vs Li/Li<sup>+</sup>. All scale bars are 1 μm. (j) Statistical data showing the average change in height of the three different types of pillars during lithiation. The average heights of the  $\langle 100 \rangle$  and  $\langle 111 \rangle$  pillars shrink after partial lithiation (120 mV) and then slightly increase after full lithiation (10 mV), while the average height of the  $\langle 110 \rangle$  pillars increases after both partial and full lithiation. (k) Statistical data showing the average change in volume after partial and full lithiation. The three types of pillars all undergo a similar amount of volume expansion.

wafers along  $\{111\}$  planes after hydrogen implantation.<sup>26</sup> Hydrogen and Li are both small atoms in the same column of the Periodic Table and could be expected to exhibit similar diffusion behavior in the Si lattice; this is supported by our study of Li diffusion in a Si wafer (Figure S3, see Supporting

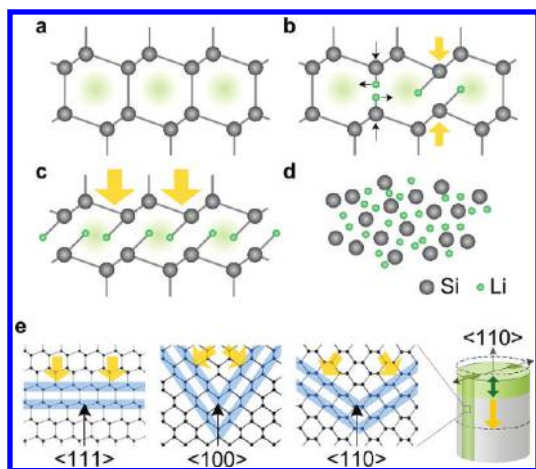


**Figure 4.** Schematic explaining height changes of Si nanopillars. (a–c) View of the diamond cubic structure along a  $\langle 110 \rangle$  direction. (a) Li diffuses along the  $\langle 110 \rangle$  ion channels. (b) A Si–Si bond between  $\{111\}$  planes is broken and replaced by two Li–Si bonds, and the Li atoms slide past each other into stable positions as the concentration of Li increases. (c) The propagation of Si–Si bond breaking and Li atom sliding induces collapse of the  $\{111\}$  planes. (d) Finally, the crystalline silicon becomes an amorphous Li–Si alloy. (e) Schematics of the diamond cubic structure viewed along a  $\langle 110 \rangle$  direction showing the orientation of  $\{111\}$  planes (blue) in relation to the axial directions of the three different nanopillars.  $\{111\}$  plane collapse in the  $\langle 111 \rangle$  nanopillars results in axial shrinkage because the  $\{111\}$  planes are perpendicular to the axis. The plane collapse causes a less significant height decrease in  $\langle 100 \rangle$  nanopillars since the  $\{111\}$  planes are inclined to the axis. Although the  $\langle 110 \rangle$  nanopillars also have inclined  $\{111\}$  planes, the observed height increase is suggested to be due to growth along the axis of the Li–Si phase at the top of the nanopillar due to the  $\langle 110 \rangle$  ion channel along the nanopillar axis. This is illustrated in the rightmost schematic in (e), where the top of the  $\langle 110 \rangle$  oriented nanopillar expands upward due to amorphization during lithiation even though the  $\{111\}$  planes collapse in the bulk of the nanopillar.

Information for more details). With this in mind, the schematics in Figure 4, which show the Si lattice along the  $\langle 110 \rangle$  direction, illustrate how we suggest the  $\{111\}$  planes collapse (Figure 4a–d) and the height of the pillars change (Figure 4e). The whole process involves three stages with increasing degree of lithiation. In stage I, Li diffuses along the  $\langle 110 \rangle$  ion channels and accumulates at tetrahedral sites between  $\{111\}$  planes (highlighted as greenish regions in Figure 4a) because this is the most stable position for Li ion insertion, as shown in a previous study.<sup>19,27</sup> In stage II, as the concentration of Li increases, the Si–Si bonds between  $\{111\}$  planes are broken, and a Li atom makes a new bond with each of the two “free” Si atoms. The two Li atoms repel since they are both positively charged, so they slide past each other into new stable positions along with their bonded Si atoms, as shown in Figure 4b. We suggest that the propagation of bonding and sliding along the  $\{111\}$  plane induces a slight decrease in distance between the  $\{111\}$  planes, as shown in Figure 4c. The small size of the nanopillar compared to a bulk sample could facilitate this collapse process because atomic rearrangement is less constrained by neighboring material than in the bulk. In stage III, further lithiation causes most of the Si–Si bonds to break, and the crystal structure becomes an amorphous Li–Si alloy (Figure 4d). Overall, this mechanism would cause the axial shrinking observed in the  $\langle 111 \rangle$  oriented nanopillars during stage

II since the  $\{111\}$  plane collapse occurs along the axial direction, as shown in Figure 4e. The  $\langle 100 \rangle$  nanopillars show less significant length contraction during stage II because the  $\{111\}$  planes are at an angle to the axial direction, so the effect of the plane collapse on the nanopillar length is less pronounced (Figure 4e). After decreasing in stage II, the average heights of the  $\langle 111 \rangle$  and  $\langle 100 \rangle$  nanopillars slightly increase in stage III with further lithiation; we attribute this to volume expansion after the crystal has amorphized. In contrast, the average height of the  $\langle 110 \rangle$  nanopillars is observed to increase when partially and fully lithiated even though these nanopillars also have  $\{111\}$  planes inclined to the axial direction (Figure 4e). We suggest that the  $\langle 110 \rangle$  ion channel along the nanopillar axis causes the amorphous Li–Si phase to grow outward at the top of the nanopillar in a similar manner to the expansion of the Li–Si phase along  $\langle 110 \rangle$  cross-sectional directions (Figure 1). This would cause the  $\langle 110 \rangle$  nanopillars to increase in height even if the inclined  $\{111\}$  planes undergo collapse, as shown in the schematic in Figure 4e.

In summary, we have discovered anomalous shape changes of crystalline Si nanostructures during lithiation through multi-dimensional observation and have proposed mechanisms that give insight into the fundamental physical mechanisms governing the process. During the initial stages of lithiation, we suggest that Li enters the crystalline Si nanostructure through  $\langle 110 \rangle$  ion channels and induces the collapse of some  $\{111\}$  planes by breaking Si–Si bonds; this causes the observed decrease in height of the  $\langle 111 \rangle$  and  $\langle 100 \rangle$  axially oriented nanopillars. In addition, the amorphous phase begins to form at the surface of the  $\langle 110 \rangle$  ion channels where the Li concentration is highest, and it grows to form the cross, ellipse, and hexagonal cross-sectional shapes of the  $\langle 100 \rangle$ ,  $\langle 110 \rangle$ , and  $\langle 111 \rangle$  pillars, respectively. These findings provide an important understanding of the structural evolution during electrochemical lithiation of Si nanostructures. This can be a guide for developing higher performance Si anodes by, for example, increasing the prevalence of  $\{110\}$  facets to promote fast diffusion of Li ions for high power and by maintaining the partial crystallinity of Si for longer cycle life.

## ■ ASSOCIATED CONTENT

Supporting Information. Additional information provided. This material is available free of charge via the Internet at <http://pubs.acs.org>.

## ■ AUTHOR INFORMATION

### Corresponding Author

\*E-mail: [yicui@stanford.edu](mailto:yicui@stanford.edu).

### Present Addresses

<sup>†</sup>Department of Energy, Environment, Water and Sustainability, Korea Advanced Institute of Science and Technology, 37311 Guseong Dong, Yuseong Gu, Daejeon 305-701, Republic of Korea.

### Author Contributions

<sup>‡</sup>These authors contributed equally to this work.

## ■ ACKNOWLEDGMENT

This work is partially supported by the Department of Energy, Office of Basic Energy Sciences, Division of Materials Sciences and Engineering under contract DE-AC02-76SF0051 through

the SLAC National Accelerator Laboratory LDRD project. Y.C. acknowledges support from the King Abdullah University of Science and Technology (KAUST) Investigator Award (No. KUS-I1-001-12). S.W.L. acknowledges support from KAUST (Award No. KUK-F1-038-02). M.T.M. acknowledges support from the Chevron Stanford Graduate Fellowship, the National Defense Science and Engineering Graduate Fellowship, and the National Science Foundation Graduate Fellowship. J.W. C. acknowledges the National Research Foundation of Korea Grant funded by the Korean Government (MEST) for the financial support through the Secondary Battery Program (NRF-2010-0029031) and the World Class University Program for the financial support (R-31-2008-000-10055-0).

(26) Tong, Q. Y.; Gutjahr, K.; Hopfe, S.; Gosele, U.; Lee, T. H. *Appl. Phys. Lett.* **1997**, *70* (11), 1390–1392.

(27) Wan, W. H.; Zhang, Q. F.; Cui, Y.; Wang, E. G. *J. Phys.: Condens. Matter* **2010**, *22*, 415501.

## REFERENCES

- (1) Armand, M.; Tarascon, J. M. *Nature* **2008**, *451* (7179), 652–657.
- (2) Whittingham, M. S. *MRS Bull.* **2008**, *33* (4), 411–419.
- (3) Boukamp, B. A.; Lesh, G. C.; Huggins, R. A. *J. Electrochem. Soc.* **1981**, *128* (4), 725–729.
- (4) Kasavajula, U.; Wang, C. S.; Appleby, A. J. *J. Power Sources* **2007**, *163* (2), 1003–1039.
- (5) Beaulieu, L. Y.; Eberman, K. W.; Turner, R. L.; Krause, L. J.; Dahn, J. R. *Electrochem. Solid-State Lett.* **2001**, *4* (9), A137–A140.
- (6) Chan, C. K.; Peng, H. L.; Liu, G.; McIlwrath, K.; Zhang, X. F.; Huggins, R. A.; Cui, Y. *Nat. Nanotechnol.* **2008**, *3* (1), 31–35.
- (7) Magasinski, A.; Dixon, P.; Hertzberg, B.; Kvit, A.; Ayala, J.; Yushin, G. *Nat. Mater.* **2010**, *9* (4), 353–358.
- (8) Cui, L. F.; Ruffo, R.; Chan, C. K.; Peng, H. L.; Cui, Y. *Nano Lett.* **2009**, *9* (1), 491–495.
- (9) Kim, H.; Seo, M.; Park, M. H.; Cho, J. *Angew. Chem., Int. Ed.* **2010**, *49* (12), 2146–2149.
- (10) Song, T.; Xia, J. L.; Lee, J. H.; Lee, D. H.; Kwon, M. S.; Choi, J. M.; Wu, J.; Doo, S. K.; Chang, H.; Il Park, W.; Zang, D. S.; Kim, H.; Huang, Y. G.; Hwang, K. C.; Rogers, J. A.; Paik, U. *Nano Lett.* **2010**, *10* (5), 1710–1716.
- (11) Kim, H.; Han, B.; Choo, J.; Cho, J. *Angew. Chem., Int. Ed.* **2008**, *47* (52), 10151–10154.
- (12) Deshpande, R.; Cheng, Y. T.; Verbrugge, M. W. *J. Power Sources* **2010**, *195* (15), 5081–5088.
- (13) Limthongkul, P.; Jang, Y. I.; Dudney, N. J.; Chiang, Y. M. *Acta Mater.* **2003**, *51* (4), 1103–1113.
- (14) Chan, C. K.; Ruffo, R.; Hong, S. S.; Huggins, R. A.; Cui, Y. *J. Power Sources* **2009**, *189* (1), 34–39.
- (15) Hatchard, T. D.; Dahn, J. R. *J. Electrochem. Soc.* **2004**, *151* (6), A838–A842.
- (16) Li, H.; Huang, X. J.; Chen, L. Q.; Zhou, G. W.; Zhang, Z.; Yu, D. P.; Mo, Y. J.; Pei, N. *Solid State Ionics* **2000**, *135* (1–4), 181–191.
- (17) Key, B.; Bhattacharyya, R.; Morcrette, M.; Seznec, V.; Tarascon, J. M.; Grey, C. P. *J. Am. Chem. Soc.* **2009**, *131* (26), 9239–9249.
- (18) Chan, T. L.; Chelikowsky, J. R. *Nano Lett.* **2010**, *10* (3), 821–825.
- (19) Zhang, Q. F.; Zhang, W. X.; Wan, W. H.; Cui, Y.; Wang, E. G. *Nano Lett.* **2010**, *10* (9), 3243–3249.
- (20) Hsu, C. M.; Connor, S. T.; Tang, M. X.; Cui, Y. *Appl. Phys. Lett.* **2008**, *93*, 133109.
- (21) Chang, C. L.; Wang, Y. F.; Kanamori, Y.; Shih, J. J.; Kawai, Y.; Lee, C. K.; Wu, K. C.; Esashi, M. *J. Micromech. Microeng.* **2005**, *15* (3), 580–585.
- (22) Campbell, S. A. *The Science and Engineering of Microelectronic Fabrication*, 2nd ed.; Oxford University Press: New York, 2001.
- (23) Terreaux, B. *Phys. Status Solidi A* **2007**, *204* (7), 2129–2184.
- (24) Vandewalle, C. G.; Denteneer, P. J. H.; Baryam, Y.; Pantelides, S. T. *Phys. Rev. B* **1989**, *39* (15), 10791–10808.
- (25) Martsinovich, N.; Heggge, M. I.; Ewels, C. P. *J. Phys.: Condens. Matter* **2003**, *15* (39), S2815–S2824.